Microstructural study of the deformation zones around a penetrating coned tip in silty soil

P. Paniagua, A.S. Gylland & S. Nordal
Norwegian University of Science and Technology (NTNU), Trondheim, Norway

J. Fonseca
City University London, London, United Kingdom

ABSTRACT: The change in soil microstructure around the penetrating probe during a cone penetration test is investigated. Backscattered electron images of polished thin sections prepared from frozen samples at the end of penetration are used. The images have a spatial resolution of 0.4 µm/pixel that allow a clear identification of grains and pore spaces. The statistical distribution of the change of particles orientation is analyzed for the zones around the cone tip and the shaft. Quantitative analysis of the change in porosity near the penetrating object is investigated. An increase in porosity and a decrease in the anisotropy of particle orientations from the cone and further out confirm that the soil deformation during CPTU in silt is a combination of compaction and dilative behavior that might influence the pore pressure distribution during penetration.

1 INTRODUCTION

1.1 *Motivation and scope*

The cone penetration test (CPT) is a field test which consists on pushing a cone on the end of a cylindrical probe into the ground. The conventional probe diameter is 35.7 mm and the conventional pushing rate is 20 mm/s. Measurements of cone tip resistance to penetration and shaft friction are recorded. If in addition the pore water pressure is measured behind the cone shoulder (u_2 position), the test is called CPTU. The objectives of the test are to identify soil material layering and geotechnical parameters for design.

Interpretation methods for CPT or CPTU, using continuum mechanics concepts, are based on one of two extremes: drained behavior in sands and undrained behavior in clay. In the case of intermediate soils like silts, penetration occurs under partially drained conditions (Lunne et al. 1997). Understanding the partial drainage behavior of silts from the particle-scale physics can help to determine the macroscopic behavior of this granular material.

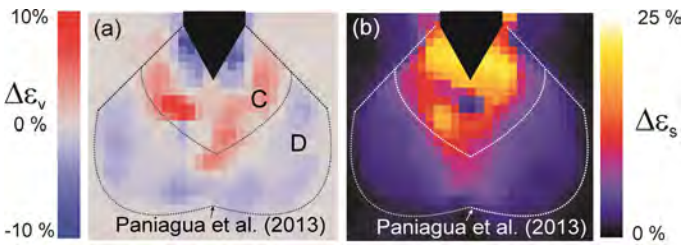

Figure 1. (a) Incremental volumetric strains and (b) incremental shear strains for a penetration increment of 5 mm (Paniagua et al. 2013). C: compaction and D: dilation.

The present study investigates the change in the microstructure (or fabric) of the soil surrounding the probe during CPTU penetration. Fabric quantification based on particle orientation and changes in porosity near the penetrating object are performed. The aim is to improve our understanding of the micro mechanisms underlying soil deformation during CPTU and the drainage condition during penetration in silts.

1.2 *Deformation zone around a penetrating probe*

The soil displacement around a penetrating object has been studied before by different techniques in plane strain (Muromachi 1974; White et al. 2004), semi-cylindrical (Roy et al. 1974; Liu 2010) and axisymmetrical conditions (Robinsky & Morrison 1964; Yasafuku & Hyde 1995; Kobayashi & Fukagawa 2003; van Nes 2004; Ngan-Tillard et al. 2005; Morita et al. 2007; Kikuchi et al. 2010). A general compression failure mode for shallow penetration is observed in contrast to a more radial failure pattern for deep penetration. Johnson & Schneebeli (1999) and Johnson (2003) presented a statistical micromechanical theory of cone penetration in granular material after studying the mechanical response of snow during microcone penetration.

Paniagua et al. (2012) presented observations and measurements of soil (silt) behavior around a CPT in laboratory tests using two experimental setups: one involving freezing the sample after penetration to preserve deformation patterns and failure features, and one involving computerized tomography. Verti-

cal compression below the tip and volumetric expansion behind the shoulder was observed. Distinct shear structures appear along the shaft.

Laboratory scale CPTs on Vassfjellet silt investigated by x-ray computed tomography (micro CT) and 3D Digital Image Correlation (3D-DIC) were done by Paniagua et al. (2013). The failure pattern observed has two clearly distinguishable zones of compaction and dilation respectively under the tip with distinct zones of shear along the shaft. They suggest that the failure mechanism is most likely not just a uniform plastic reshaping. Figure 1a and Figure 1b show the incremental volumetric strains and the incremental shear strains maps, respectively, obtained by 3D-DIC analysis.

2 MATERIAL AND METHODS

2.1 *Vassfjellet silt*

The silt studied is a non-plastic uniform silt from Vassfjellet, Klæbu, Norway. It has 94% of its grains lower than 74 µm and a clay content of 2.5%. The material has a maximum void ratio of 1.46, obtained by allowing a slurry to settle in a graduated cylinder (Bradshaw & Baxter, 2007), and a minimum void ratio of 0.56, obtained by the modified compaction method for fine grained soils (Sridharan & Sivapullaiah, 2005) which resembles a Proctor compaction test. A maximum dry density ($\rho_{d\text{-}max}$) of 1.6 g/cm^3 was found at 23% optimum water content and 95% saturation. Mineralogy testing showed 35% muscovite, 27% quartz, 18% chlorite, 15% feldspar and 5% actinolite. High dilatant behavior was observed in samples tested in undrained triaxial tests (isotropic consolidated) at its maximum density (Kim, 2012) and a friction angle φ' of 32° was found.

Table 1. Specimens characteristics.

Specimen	MMT01	MMT02	MMT03
Top pressure p_o' [kPa]	0	40	40
Cone diameter d_c[mm]	35.7	35.7	20.0
Soil cylinder diameter [mm]	220	220	100
Plexiglas cylinder diameter [mm]	245	245	140

Figure 2 shows a backscattered electron image from an electron probe micro analysis (EPMA) scan of the Vassfjellet silt.

2.2 *Test program and equipment*

The present study makes use of the experimental work presented in Paniagua et al. (2012). The specimen's sizes are detailed in Table 1. The specimens were prepared by the modified moist tamping (MMT) method (Bradshaw & Baxter, 2007) and saturated from the bottom to limit air bubbles formation. The samples had a dry density (ρ_d) of 1.4 g/cm^3, 60% relative density (D_r) and 47% water content. A total of three samples have been studied. Their specifications are detailed in Table 1.

In general, the specimens were built inside a Plexiglas cylinder padded with a layer of neoprene padding. The paddings were used to compensate for the effect of the boundary closeness and account for the compressibility of the lacking surrounding soil. After preparation, the samples were preloaded on top and thereafter tested while attempting to maintain the vertical top pressures. The samples were progressively penetrated at a standard rate of 20 mm/s. Two different probes diameters were used (Table 1). After the probe penetration, the samples were frozen with the cone inside following the technique proposed by Paniagua et al. (2012). This allows removing the molding forms and the cone, and cutting the frozen sample through its center. After sample cutting, the frozen blocks were carefully oven dried based on a previous evaluation of drying techniques.

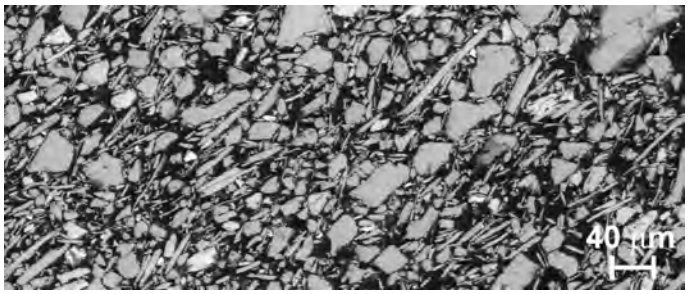

Figure 2. Backscattered electron image from EPMA scan of the Vassfjellet silt.

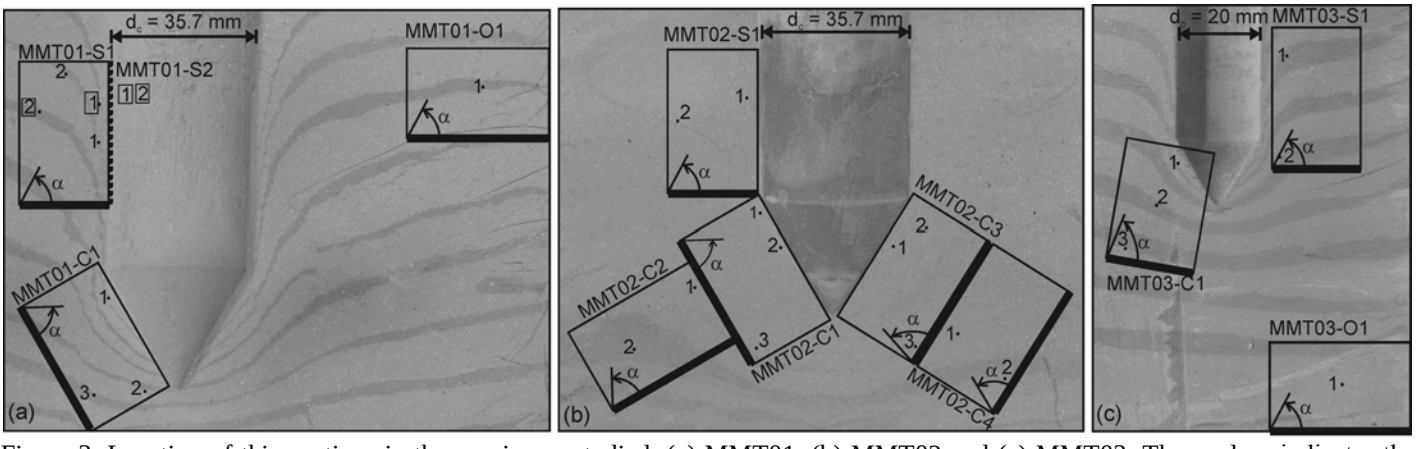

Figure 3. Location of thin sections in the specimens studied: (a) MMT01, (b) MMT02 and (c) MMT03. The angle α indicates the reference plane (shown as a thicker line) for measuring the particle orientations in the rose diagrams. The numbered dots indicate the regions where EPMA images were obtained.

2.3 *Production of thin sections*

Thin sections of 30 µm thickness, 36x22 mm, were prepared from the dried samples to study the deformation zones around the cone and shaft. Epoxy resin impregnation (Gylland et al. 2013) was done either in carefully carved smaller pieces or directly in the areas around the cone and shaft. A low viscosity resin was used and it is believed that the soil microstructure was not disturbed by impregnation. Resin impregnation of soil for fabric inspection was successful used in previous studies, e.g. Fonseca et al (2012). Figure 3 shows the location of the thin sections in the specimens.

2.4 *Microscopy equipment*

The thin sections were firstly inspected using polarized light microscope (Nesse, 2011) to define specific areas of interest for detailed analysis by EPMA. A JEOL JXA-8500F Electron Probe Micro analyzer (EPMA) was used to get backscattered electron images from the specific areas defined in the thin sections. These areas are marked in Figure 3 with black dots. They are distributed according to the deformation zones observed by Paniagua et al. (2013).

3 EXPERIMENTAL RESULTS

3.1 *Porosity analysis*

The backscattered electron images have a spatial resolution of 0.4 µm/pixel which allows a clear identification of the grains and pore spaces. The images were segmented using the threshold method proposed by Otsu (1979), which divides the histogram in two classes and the threshold is the value that minimized the within-class (Fonseca et al. 2012). The algorithm has been implemented in ImageJ 1.48g (Rasband 2013).

The porosities are studied by defining a 2D void ratio which relates the amount of pixels corresponding to pore spaces to the amount of pixels corresponding to grains. The resultant void ratio values come from an average of subregions defined in the EPMA image. Figure 4 shows the variation of void ratio values with the normalized distance either r/r_c or x/r_c, where r_c is the cone radius, r is measured from the intersecting point between the vertical cone axis and the horizontal shoulder axis, x is the horizontal distance from the cone vertical axis.

3.2 *Orientation analysis*

By observation of the EPMA images, two main grain classes can be distinguished: bulky grains and flaky grains. Flaky grains are defined as those grains that have a minor axis smaller than 5 µm and therefore show an aspect ratio (AR) lower than 0.45. The AR is defined as the ratio between the minor and the major axis lengths, (e.g., $AR_{sphere} = 1$). Bulky grains are then those that show an AR > 0.45. Figure 5a presents examples of flaky and bulky grains. A manual technique was used to identify the points defining the major and minor axis of the grains. Coordinates were selected for each grain using ImageJ as detailed in Fonseca et al (2013c). The grains that were smaller than 5 µm (which represent a 12% of the total weight) were not accounted for the analysis.

The regions for particle orientation analysis coincide with the zones used for the porosity study. The coordinates for all the grains in the region of analysis were imported into MATLAB (Mathworks) and a procedure similar to the one presented by Fonseca et al. (2013a, b) was followed.

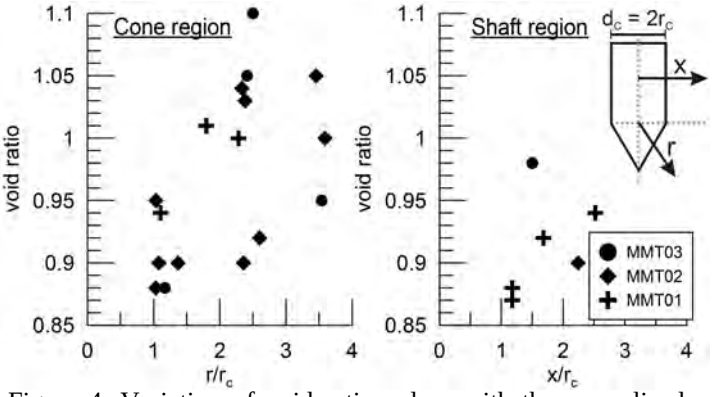

Figure 4. Variation of void ratio values with the normalized distance either r/r_c or x/r_c in the different specimens.

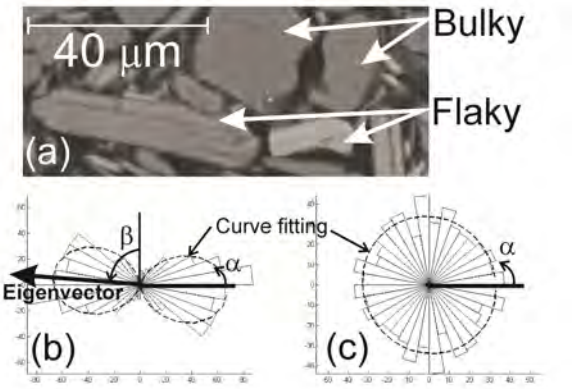

Figure 5. (a) Examples of flaky and bulky grains. (b) Definition of angle β giving the eigenvector inclination to vertical axis and examples of an anisotropic rose diagram for flaky grains in MMT02-C1-1 and (c) an isotropic rose diagram for MMT02-C2-2. The complete diagrams are presented to illustrate the curve fitting.

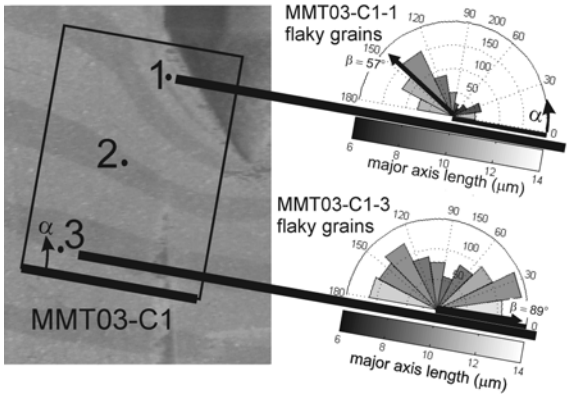

Figure 6. Example for orientation of the rose diagrams following the thin section orientation.

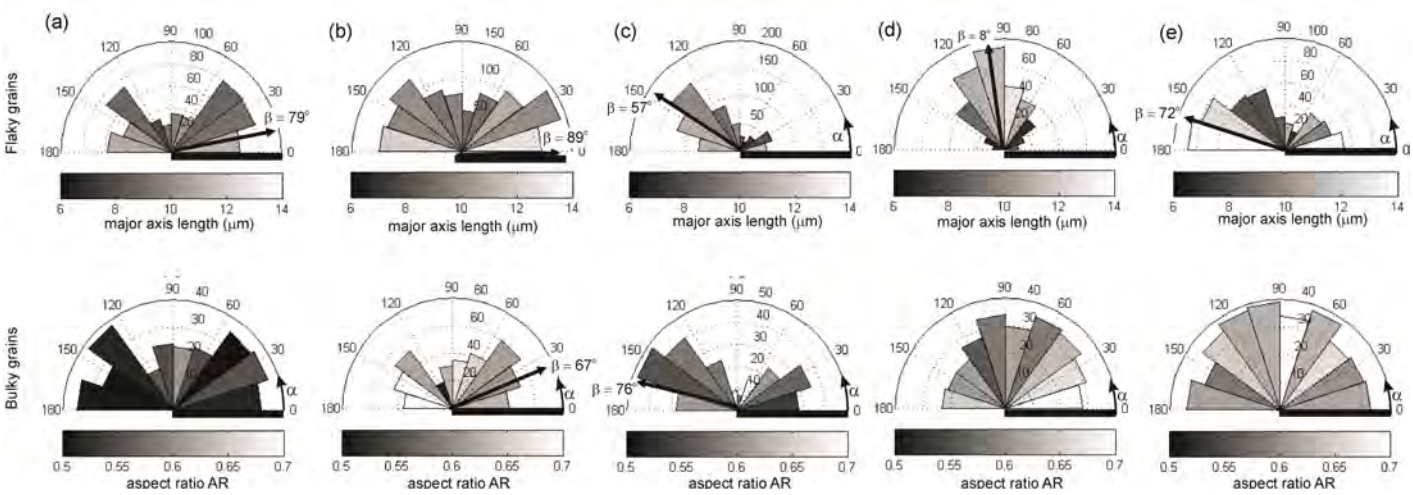

Figure 7. Rose diagrams of particle orientations for locations: (a) MMT03-O1-1, (b) MMT03-C1-3, (c) MMT03-C1-1, (d) MMT02-S1-1 and (e) MMT02-S1-2. The eigenvector associated with the major eigenvalue is indicated by the arrow and its angle β. The thick line is the reference plane for angle α.

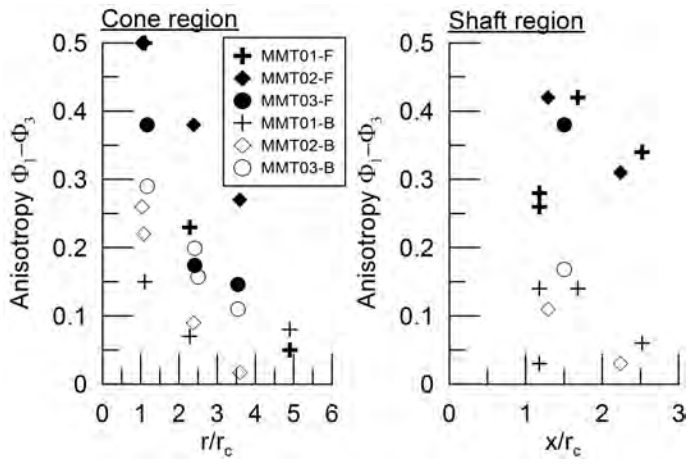

Figure 8. Variation of anisotropy with r/r_c or x/r_c for flaky (F) and bulky (B) grains in the different specimens.

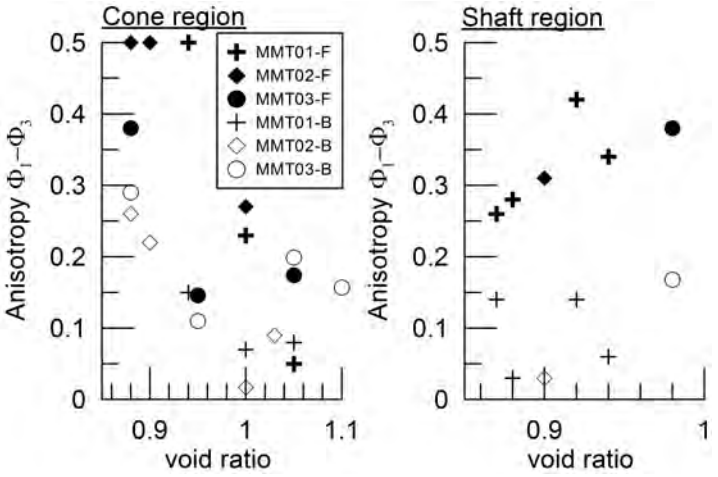

Figure 9. Variation of anisotropy with void ratio for flaky (F) and bulky (B) grains in the different specimens

A data set was collected for each specimen in terms of flaky and bulky grains and the statistical distribution of the vectors defining the particle orientation was quantified as described in the following paragraphs. The directional distribution of particle orientation (angle α) can be visualized using 2D rose diagrams, or angular histograms, (e.g., Fonseca et al. 2013a). As shown in Figure 7 each histogram bin represents an angular interval in respect to a defined plane shown in Figure 3 (angle α). Figure 6 illustrates how the rose diagrams must be oriented according to the thin section orientation. Each bin is shaded according to the major axis length (in μm) for the flaky grains and the AR for the bulky grains, respectively. Each particle has a defined orientation vector without a specific direction, i.e. an orientation of 30° is equivalent to an orientation of 210°, and therefore, only half of the plane is considered

The vector distribution from the rose diagrams was further analyzed by defining an inclination angle β measured with respect to the plane perpendicular to the rose diagram reference plane (Fig. 5b). The angle β is the orientation of the eigenvector associated with the major eigenvalue which gives an indication of the preferred fabric orientation. The maximum and minimum eigenvalues are calculated for the fabric tensor of the vectors defining the particle orientation as described in Fonseca et al. (2013a).

The distribution of the particle orientation vectors can be represented by a Fourier series (Rothenburg and Bathurst, 1989). The vectors distribution and its fitted Fourier series is shown in Figure 5 for two extreme cases; Figure 5b shows a case of high anisotropy and Figure 5c is more isotropic. The anisotropy was quantified by considering the difference between the major and minor eigenvalues of the fabric tensor, i.e. Φ_1- Φ_3 (Fonseca et al. 2013a). For more anisotropic distributions, the difference between the major and minor eigenvalues of the fabric tensor is close to 0.5 and when the values are close to zero, the distribution is isotropic and the Fourier fitting has a more circular shape (Rothenburg and Bathurst, 1989). An anisotropic distribution is characterized by a predominant particle alignment which is given by the angle β. In an isotropic distribution, the particles tend to align in random directions and the angle β becomes less meaningful.

Table 2 presents the locations of the regions of analysis and the angle β for flaky and bulky grains. The number of grains used is the analysis is also in-

dicated. A study regarding the influence of the sample size (i.e. number of grains used in the analysis) performed in the sections MMT03-C1-1, MMT03-C1-2 and MMT03-C1-3 indicated that an increase in the number of flaky grains produced very similar results, therefore this sample size is considered representative for the analysis.

Table 2. Summary of the rose diagrams analysis.

Specimen	Location	r/r_c x/r_c	Flaky grains No.	Flaky grains β[°]	Bulky grains No.	Bulky grains β[°]
MMT01	O1-1	4.90	423	---	256	---
	C1-1	1.10	333	-78	256	---
	C1-3	2.28	318	-37	343	---
	S1-1	1.18	352	37	379	---
	S1-2	1.68	226	47	285	---
	S2-2	2.52	249	-49	433	---
	S2-1	1.18	335	-9	366	---
MMT02	C2-2	3.59	813	39	605	---
	C1-1	1.08	611	85	512	-78
	C1-2	1.03	363	-73	241	-75
	C1-3	2.38	389	-43	358	---
	S1-1	1.29	343	8	293	---
	S1-2	2.24	513	72	347	---
MMT03	O1-1	6.44	546	-79	291	---
	S1-1	1.50	513	-41	238	---
	S1-2	1.50	435	-44	241	---
	C1-1	1.17	688	57	263	76
	C1-2	2.41	963	78	401	-71
	C1-3	3.54	1024	-89	422	-67

Figure 7 shows some selected rose diagrams with the indication of the angle β. Referring to flaky grains, the diagrams indicate the evolution of particle orientation starting in MMT03-O1-1 (β = 79°) with a horizontal orientation due to sample construction, towards MMT03-C1-3 with more isotropic distribution and MMT03-C1-1 (β = 57°) with an anisotropic distribution and grains getting align parallel to the cone face. Near the shaft, the particles orient almost vertically (MMT02-S1-1) respect to the more horizontal orientation further out (MMT02-S1-2). The thin sections were originally preoriented as shown in Figure 3.

Figure 8 shows the variation of the anisotropy value given by Φ_1- Φ_3 with r/r_c or x/r_c. In the cone region, a general trend of decrease in anisotropy with an increase in distance from the cone is observed. In the shaft region, there is no clear trend.

4 DISCUSSION

4.1 *Observations regarding micro behavior*

The porosity analysis (Fig. 4) shows that there is an increase in void ratio with an increase of the radial distance from the cone tip and the horizontal distance from the shaft. These results coincide with the ones reported by Paniagua et al. (2013) regarding the zones of compaction near the cone and dilation further below (Fig. 1).

In respect to the grain morphology, the results obtained indicate that the largest flaky grains tend to respond more rapidly showing a clearer reorientation following the deformation imposed by the cone. The bulky grains with low AR tend to show a similar behavior, however those with high AR show a later response due to a more restricted area for possible movement.

The statistical distribution of the particle orientation vectors using the rose diagrams characterized by its eigenvector orientation (angle β) and anisotropy value suggest the following:

- Flaky grains tend to align more horizontally during sample preparation, which is the most stable position when a tamping method is used (Fonseca et al. 2013a). MMT03-O1-1 confirms this trend (Fig. 7a). Flaky grains are more prone to re-orientate under the deformation imposed as shown by the higher anisotropy values (Fig. 8). Therefore, it is convenient to study the particle orientation based on its indications. However, other effects that cannot be quantified in this analysis (like shear reorientation) might be present.
- Zones that are far from the cone (like MMT01-O1-1 and MMT03-O1-1) indicate that the longest grains are horizontal which means they are not to any high extent influenced by cone penetration.
- Near the cone, large flaky grains orient parallel to the cone face. Along the shaft, these grains align more vertically (β tends to 0°).
- Bulky grains present more isotropic distributions and the physical meaning of the angle β is less significant. The general trend is that bulky grains with high AR tend to re-orient in the same direction that the longest flaky grains and the low AR bulky grains tend to re-orient perpendicular to the main flaky grains orientation.

4.2 *Observations regarding macro behavior*

The tests studied presented two macro variables: cone size and top pressure.

Regarding the cone size influence, by studying the variation of void ratio with the normalized radial distance r/d_{50} (where d_{50} = 0.012 mm) in specimens MMT02 and MMT03, it is observed that higher porosities are reached at a shorter distance from the cone tip in MMT03, which may indicate a smaller zone of influence due to penetration for a smaller diameter. However, the extension of the influence zone as a result of different cone diameter cannot be defined due to lack of data available. If instead of the porosity, the anisotropy of the vectors distribution for flaky grains in MMT02 and MMT03 is studied, a similar tendency is observed since the lower anisotropic values are found for MMT03 at shorter distance from the cone tip.

Regarding the top pressure influence, by comparing the angle β for MMT01 and MMT02 in the

zones along the shaft, a larger difference of the angle given by the major eigenvector is observed in the specimen with high top pressures ($\beta_{MMT02\text{-}S1\text{-}3}$ = 72° > $\beta_{MMT02\text{-}S1\text{-}1}$ = 9°) than in the specimen with low top pressures ($\beta_{MMT01\text{-}S1\text{-}2}$ = 47°~$\beta_{MMT01\text{-}S1\text{-}1}$ = 37°). This means that the influence zone along the shaft is smaller for the specimen with higher pressures on top. An angle β closer to 90° indicates a horizontal orientation which is close to its original orientation according to sample construction (Fig. 7a).

Around the cone, a similar behavior is observed, since the rose diagrams in MMT02 show a higher rate of isotropy when increase the distance r from the cone. The zone of failure influenced by the cone extends less when high pressures on top are added. This observation was also pointed out by Paniagua et al. (2013).

4.3 *Kinematics of deformation*

In order to link the micro and macro behavior, the variation of anisotropy with void ratio has been plotted in Figure 9. Two different plots are shown indicating the results for either the cone influence zone or the shaft influence zone.

It is observed that in the cone area there is a strong relation between the decrease in anisotropy and increase in void ratio in flaky grains. The bulky grains show a similar tendency, but not as strong as the one shown by the flaky grains. This might indicate that an isotropic distribution may be related to a more dilative response of the material. In other words, the material under compaction around the cone is forced to rotate following the cone movement. An isotropic distribution means that the flaky grains are oriented evenly in all directions and therefore their rotation from a stable anisotropic distribution to a more random isotropic distribution will open spaces between the grains (i.e. dilation).

Along the cone shaft, a different pattern is identified since the anisotropy increases with void ratio in the case of flaky grains. Bulky grains do not show a strong dependency on the cone movement. This suggests that the flaky grains align along the cone shaft and show higher void ratios. The shear structures (fractures) observed by Paniagua et al. (2012) and Paniagua et al. (2013) might contribute to the increase in void ratio in the closest area to the cone which shows high anisotropy.

Figure 10a shows a schematic representation of the kinematics of deformation after the results obtained in the present analysis. In general the deformation followed by the particles tends to be similar regardless the cone size and the top pressure imposed in the soil. These macro variables have more influence in the extension of the influence zone along the cone tip and probe shaft.

Paniagua et al. (2013) observed that for a sample with high pressures on top the influenced failure zone around the cone extends horizontally to about $2d_c$ from the axis of the probe and to $2d_c$ (from the tip), d_c being the probe or cone diameter. The influenced area increases to a maximum of $3d_c$ horizontally and $3d_c$ vertically in a sample with low overburden pressure. Comparing the failure extension in the sample with high overburden from Paniagua et al. (2013) with the porosities around the cone for MMT03 (Fig. 10b), one can see that the limit between the compaction and dilative zone is about a void ratio value of 1.0. More data is needed to clearly define the size of the influence zone from micro observations; however, the presence of a compaction and dilation zone coincides with Paniagua et al. (2013).

As stated by Paniagua et al. (2013) regarding the interaction between the compressive and the dilative zones around the cone tip, in the case of saturated soil, water may move locally from an observed compressive to a neighboring observed dilative zone, creating a short drainage path. Following the observation of the present work, the presence of the dilative and compressive zones around the cone is visible. Furthermore, their relation with the particle orientation shows that the dilation might be caused by the reorientation of the flaky grains and the opening of new pore spaces that will create underpressure. Along the cone shaft, the suction will be caused by the reorientation of the flaky grains and the shear structures (fractures) created by the cone passing, as explained by Paniagua et al. (2013), in addition to the elongation caused by continuous penetration (as stated also by Paniagua et al. 2012).

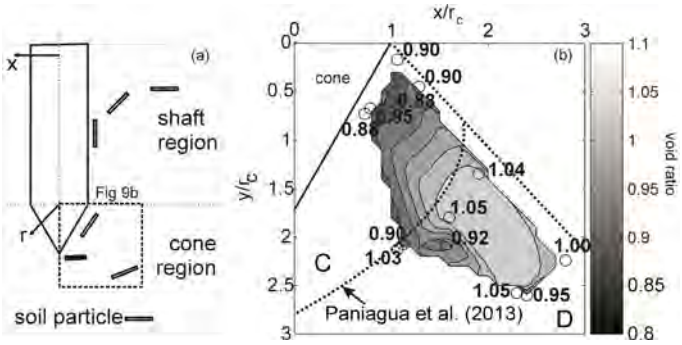

Figure 10. (a) Schematic representation of the kinematics of deformation during CPTU after the present microstructural study. (b) Comparison of the extension of the influence zone around the cone proposed by Paniagua et al. (2013) and the results from the present analysis for a sample with top pressure. A cubic interpolation method has been applied to obtain the shading in void ratio. C: compaction and D: dilation.

5 CONCLUSIONS

The soil deformation around the probe during the cone penetration test has been studied using a micromechanics approach. The analysis of the change in porosity and particle orientations has shown that the response of Vassfjellet silt during cone penetra-

tion is a combination of compaction and dilation. The extension of each influence area depends on the initial effective stresses surrounding the penetrating probe. The interaction between the compressive and the dilative zones is likely to influence the pore pressure distribution during penetration which explains the partial drainage behavior of this soil.

6 ACKNOWLEDGEMENTS

Workshop engineers F. Stæhli and T. Westrum at NTNU are greatly acknowledged for valuable help with construction of the testing apparatus. Engineer A. Monsøy at NTNU prepared the thin sections. The EPMA scans were performed by Engineer K. Eriksen at NTNU.

7 REFERENCES

Bradshaw, A.S. & Baxter, C.D.P. 2007. Sample preparation of silts for liquefaction testing. *Geotechnical Testing Journal* 30: 324-332.

Fonseca, J., O'Sullivan, C., Coop, M. & Lee, P.D. 2012. Non-invasive characterization of particle morphology of natural sands. *Soils and Foundations* 52 (4): 712-722.

Fonseca, J., O'Sullivan, C., Coop, M. & Lee, P.D. 2013a. Quantifying evolution soil fabric during shearing using directional parameters. *Géotechnique* 63 (6): 487-499.

Fonseca, J., O'Sullivan, C., Coop, M. & Lee, P.D. 2013b. Quantifying evolution soil fabric during shearing using scalar parameters. *Géotechnique* 63 (10): 818-829.

Fonseca, J., O'Sullivan, C., Hagira, T., Yasuda, H. and Gourlay, C.M. 2013c. In situ study granular micromechanics in semi-solid carbon steels. *Acta Materialia* 61 (11): 4169-4179.

Gylland, A., Rueslåtten, H., Jostad, H.P. & Nordal, S. 2013. Microstructural observations shear zones in sensitive clay. *Engineering Geology* 163: 75-88.

Johnson, J.B. & Schneebeli, M. 1999. Characterizing the microstructural and micromechanical properties of snow. *Cold Regions Science and Technology* 30 (1-3): 91-100.

Johnson, J.B. 2003. A statistical micromechanical theory of cone penetration in granular materials. US Army Corps of Engineers Technical Report.

Kikuchi, Y., Sato, T., Mizutani, T. & Morikawa, Y. 2010. Plugging mechanism of open-ended piles. In: Orense et al. (eds). *Soil–foundation–structure interaction*. London: Taylor & Francis.

Kim, Y. 2012. *Properties of silt and CPTU in model scale. MSc project work.* NTNU, Trondheim, Norway.

Kobayashi, T. & Fukagawa, R. 2003. Characterization of deformation process of CPT using X-ray TV imaging technology. In: Di Benedetto et al. (eds) *Third International Conference on Deformation Characteristics of Geomaterials*: 43-47. Lyon: Taylor & Francis.

Liu ,W. 2011. *Axisymetric centrifigue model of deep penetration in sand.* PhD dissertation, University of Nottingham.

Lunne, T., Robertson, P. and Powell, J. 1997. *CPT in geotechnical practice*. New York: Blackie Academic.

Morita, K. Otani, J., Mukonoki, T., Hironaka, J. & Pham, K.D. 2007. Evaluation of vertical and lateral bearing capacity mechanics of pile foundations using X-ray CT. In: Kikuchi (eds) *Advances in deep foundations.* London: Taylor & Francis.

Muromachi, T. 1974. Experimental study on application of static cone penetrometer to subsurface investigation of weak cohesive soils. *ESOPT* 2: 192–285.

Nesse, W. 2011. *Introduction to mineralogy*. Oxford University Press.

Ngan-Tillard, D. J. M., Cheng, X. H., van Nes, J. & Zitha, P. L. J. (2005). Application of x-ray computed tomography to cone penetration tests in sands. In: Mayne et al. (eds) *Geo-Frontiers 2005: Site characterization and modelling*. Reston, VA: ASCE.

Otsu, N. 1979. A threshold selection method from gray level histograms. *IEEE Transactions on Systems, Man and Cybernetics* 9 (1): 62-66.

Paniagua, P., Andó, E., Silva, M., Nordal, S. & Viggiani, G. 2013. Soil deformation around penetrating cone in silt. *Géotechnique Letters* 3: 185-191.

Paniagua, P., Gylland, A. & Nordal, S. 2012. Experimental study of deformation pattern around penetrating coned tip. In Laloui & Ferrari (eds) *Multiphysical testing soils-shales*: 227–232. Berlin: Springer.

Rasband, W. 2013. *ImageJ 1.48g*. National Institutes of Health, USA.

Robinsky, E.I & Morrison, C.F. 1964. Sand displacement and compaction around model friction piles. *Canadian Geotechnical Journal* 1:81-93.

Rothenburg, L. & Bathurst, R. J. 1989 Analytical study of induced anisotropy in idealized granular materials. *Géotechnique* 39 (4) : 601-614

Roy, M., Michaud, D., Tavenas, F., Leroueil, S. & Rochelle, P.L. 1974. The interpretation of static cone penetration test in sensitive clay. *ESOPT* 2: 323-330.

Sridharan, A & Sivapullaiah, P.V. 2005. Mini compaction test apparatus for fine grained soils. *Geotechnical Testing Journal* 28 (3): 240-246.

van Nes, J. 2004. *Application of computerized tomography to investigate strain fields caused by cone penetration in sand*. MSc dissertation. Delft University.

White, D.J. & Bolton, M.D. 2004. Displacement and strain paths during plane-strain model pile installation in sand. *Géotechnique* 54: 375-397.

Yasafuku, N. & Hyde, A.F.L. 1995. Pile end-bearing capacity in crushable sands. *Géotechnique* 45: 663-676.